Optimization and Validation of Methods for Mapping of the Radiofrequency Transmit Field at 3T

Antoine Lutti,[1]* Chloe Hutton,[1] Jürgen Finsterbusch,[2] Gunther Helms,[3] and Nikolaus Weiskopf[1]

MRI techniques such as quantitative imaging and parallel transmit require precise knowledge of the radio-frequency transmit field (B_1^+). Three published methods were optimized for robust B_1^+ mapping at 3T in the human brain: three-dimensional (3D) actual flip angle imaging (AFI), 3D echo-planar imaging (EPI), and two-dimensional (2D) stimulated echo acquisition mode (STEAM). We performed a comprehensive comparison of the methods, focusing on artifacts, reproducibility, and accuracy compared to a reference 2D double angle method. For the 3D AFI method, the addition of flow-compensated gradients for diffusion damping reduced the level of physiological artifacts and improved spoiling of transverse coherences. Correction of susceptibility-induced artifacts alleviated image distortions and improved the accuracy of the 3D EPI imaging method. For the 2D STEAM method, averaging over multiple acquisitions reduced the impact of physiological noise and a new calibration method enhanced the accuracy of the B_1^+ maps. After optimization, all methods yielded low noise B_1^+ maps (below 2 percentage units), of the nominal flip angle value (p.u.) with a systematic bias less than 5 p.u. units. Full brain coverage was obtained in less than 5 min. The 3D AFI method required minimal postprocessing and showed little sensitivity to off-resonance and physiological effects. The 3D EPI method showed the highest level of reproducibility. The 2D STEAM method was the most time-efficient technique.   Magn Reson Med 64:229–238, 2010. © 2010 Wiley-Liss, Inc.

Key words: RF mapping; quantitative MRI; flip-angle correction; B_1^+; B_1

Spatial inhomogeneities of the positive circularly polarized component (B_1^+) of radiofrequency (RF) B_1 result in the local deviations of the flip angle from its nominal value. These deviations affect quantitative MRI techniques such as perfusion (1), magnetization transfer ratio (2), and T_1, T_2 (3) imaging. In standard MRI, B_1^+ inhomogeneities lead to degradation of image contrast and uniformity, which limit the robustness of image processing techniques such as segmentation even after compensation for RF inhomogeneities has been applied (4–7). B_1^+ inhomogeneities increase with the strength of the static magnetic field (B_0) due to the

corresponding decrease in RF wavelength (8). B_1^+ inhomogeneities can be reduced using phased-array transmit coils when the local magnitude and phase of the RF field are known (9,10). This can be achieved by accurate B_1^+ mapping techniques (3,11). For most applications, it is sufficient to know the magnitude $|B_1^+|$ of B_1^+. For brevity, we will use the two terms synonymously in the following.

Robust B_1^+ mapping methods are often based on the double angle method (DAM) (12,13), where local flip angle values are estimated from the ratio of two images obtained for different nominal flip angle values. Here, incomplete longitudinal relaxation may bias the resulting flip angle maps for short pulse repetition times (TR) (13). Although compensating pulses (14) and magnetization resets (15) have been introduced in order to allow short TR acquisitions, the DAM method has mainly been implemented with $TR \geq 5 \times T_1$ in order to avoid bias due to longitudinal relaxation, resulting in long acquisition times impractical for routine in vivo applications. In order to speed up whole-brain B_1^+ mapping, the DAM method can also be implemented as a multislice technique. However, for two-dimensional (2D) acquisition schemes, B_1^+ maps are affected by inhomogeneous spin excitation across the slice (16), in-flow artifacts and through-plane blood flow. Nonlinearities between the slice profile and the nominal flip angle lead to misestimated B_1^+ maps and require accurate calibration of the relation between signal (integrated across the slice profile) and pulse amplitude (14,17,18). To overcome these problems, three-dimensional (3D) multishot methods using nonselective excitation have been introduced (19). These methods exhibit higher signal-to-noise ratios and reduced sensitivity to in-flow artifacts but increased sensitivity to motion artifacts (20).

In this work, we focused on in vivo mapping of the magnitude of B_1^+ at 3T. If the phase and magnitude of B_1^+ are required, a combination of one of the methods presented here with a fast phase mapping method based on gradient echo acquisitions can be used (21). For routine use in neuroimaging, short acquisition time (<5 min), whole-head coverage, high precision, and accuracy are desirable. From the literature, we selected three B_1^+ mapping methods that offer high time efficiency: (1) Yarnykh (22) introduced the 3D actual flip angle imaging (AFI) method based on successive fast low-angle-shot (FLASH) acquisitions at interleaved TRs that suffers from minimal spatial distortions and needs one data acquisition only. (2) Jiru and Klose obtained flip angle maps from spin-echo (SE) and stimulated echo (STE) images recorded with a 3D echo-planar imaging (EPI) scheme, allowing for very fast and efficient B_1^+ mapping (23). (3) Helms

[1]Wellcome Trust Centre for Neuroimaging, UCL Institute of Neurology, University College London, UK.

[2]Department of Systems Neuroscience, University Medical Center Hamburg-Eppendorf, Hamburg, Germany.

[3]MR-Research in Neurology and Psychiatry, University Medical Center Göttingen, Gottingen, Germany.

*Correspondence to: Antoine Lutti, Ph.D., 12 Queen Square, London WC1N 3BG, UK. E-mail: a.lutti@fil.ion.ucl.ac.uk

et al. developed a 2D stimulated echo acquisition mode (STEAM) method based on two acquisitions with two different flip-back angles that shows minimal distortions and a high efficiency. Each method was validated on individual subjects and phantoms in the original papers (18). However, B_1^+ maps were obtained at different field strengths and on different phantoms, so that any comparison between the results would be invalid. Here, we performed a multisubject comparison between the methods to assess their relative advantages, accuracy, and precision. We first optimized the three B_1^+ mapping methods for implementation at 3T. The accuracy of each technique was tested against results obtained using a modified version of the robust 2D DAM method proposed by Sled and Pike (24).

THEORY AND OPTIMIZATION

Here, we briefly review each of the methods and describe the optimizations that we performed. The exact details of the implementation are described in the Materials and Methods section.

3D AFI Method

The 3D AFI method records signal using two interleaved FLASH acquisitions with repetition times TR_1 and TR_2 (22). If longitudinal relaxation of the magnetization between the repetitions can be linearized ($TR_1 < TR_2 \ll T_1$), flip angle (α) maps can be extracted from the two resulting images using (22):

$$\alpha \approx \arccos\left(\frac{rn-1}{n-r}\right) \qquad [1]$$

where $n = TR_2/TR_1$, $r = S_2/S_1$ and S_1, S_2 are the signals acquired during TR_1 and TR_2, respectively. Spoiler gradients and RF spoiling as proposed by Nehrke (25) are applied in order to achieve spoiling of the transverse coherences between the gradient echoes.

For further improvement to previous 3D AFI implementations, we introduced flow-compensated diffusion-weighting spoiler gradients in order to improve spoiling of the transverse coherences by diffusion damping

(25,26) while keeping the level of physiologic artifacts minimal in the images.

3D EPI Method

With the method introduced by Akoka et al. (27), the local flip angles α are extracted from SE and STE signals. In the implementation of this method by Jiru and Klose (23), nonselective RF pulses and 3D multishot EPI acquisitions are used and local flip angles are obtained according to:

$$\alpha = \arccos\left(\frac{S_{STE}e^{\frac{TM}{T_1}}}{S_{SE}}\right) \qquad [2]$$

where S_{SE} and S_{STE} are the intensities of the SE and STE images and TM is the "mixing time," i.e., the time span between the spin and stimulated echoes. As local flip angle calculations are based on magnitude images, two possible values of α, i.e., $90 + \delta$ and $90 - \delta$, satisfy Eq. 2 at each voxel. The correct flip-angle values can be extracted from the repetition of the image acquisition for different values of the nominal flip angle, by a linear regression of nominal versus local flip angles (23).

In order to increase the robustness of the original method, we developed an image processing method, illustrated in Fig. 1. We used a B_0 map (acquired using a double gradient-echo FLASH acquisition) to correct susceptibility-induced geometric distortions of the B_1^+ maps (based on EPI acquisitions) following the method described in Hutton et al. (28). Following the linear regression described above, the square root of the residual mean square (RMS) of the fit was calculated at each voxel and divided by the number of nominal flip angle values to provide a map of error values (RMS map). Distortions were also corrected in the RMS maps, which were then used to identify voxels where a poor fit of the linear regression was present. These voxels were masked out of the B_1^+ maps, and the missing flip angle values were estimated by averaging those of the remaining neighboring voxels (*RMS padding*). Preliminary experiments showed that B_0 inhomogeneities could affect spin precession due to off-resonance effects, altering the measured effective flip angle.
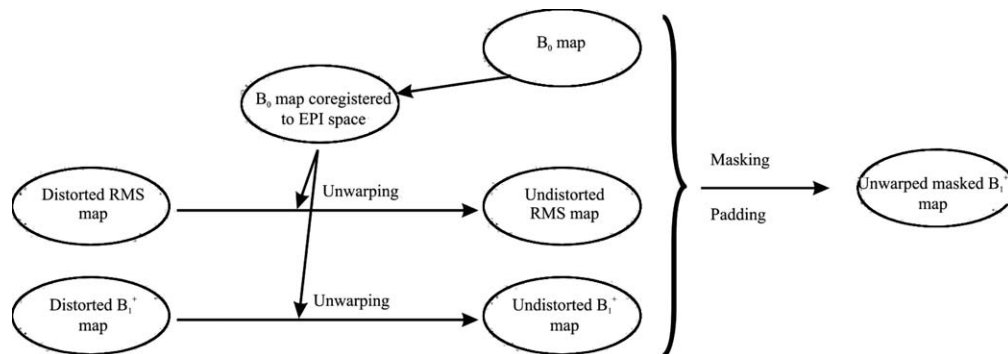

FIG. 1. Postprocessing method used for the 3D EPI acquisition scheme. Unwarping of the B_1^+ maps is followed by masking based on the local B_0 value and errors on the flip angle estimates (RMS map); 71×24 mm (600×600 DPI).

Padding was therefore also applied on the B_1^+ maps at voxels where the local B_0 field exceeded a threshold value (determined by the bandwidth of the RF pulses used in our experiment) (B_0 *padding*). The masks based on the RMS and B_0 values were effectively combined using an inclusive "or" operation before performing the padding.

$$f_T = \frac{\alpha_{\max}(\alpha_1 S_2 - \alpha_2 S_1) - \frac{1}{q}\sqrt{\alpha_1^2 S_2^2 + \alpha_2^2 S_1^2 - S_1 S_2(\alpha_1^2 + \alpha_2^2 - [q\alpha_{\max}(\alpha_2 - \alpha_1)]^2)}}{(\alpha_1^2 S_2 - \alpha_2^2 S_1)}. \qquad [3]$$

Here S_1 and S_2 are image intensities obtained for two nominal flip angles α_1 and α_2 of the "flip-back" pulse. This equation already comprises a transformation from the slice-selective signals to nonselective excitation. Equation 3 is based on a quadratic approximation of the sinusoidal flip angle dependence around its maximum:

$$S(\alpha) = S^{\max}(1 - q^2(\alpha - \alpha_{\max})^2) \qquad [4]$$

where $\alpha_{\max}$ and q are pulse-shape-dependent calibration parameters accounting for nonlinearities (shift and width) of the slice profile as the nominal flip angle is varied (18). In the original calibration method, $\alpha_{\max}$ and q are determined by comparison to a nonselective flip-back pulse in a separate fully relaxed experiment on a phantom.

In this work, calibration of the nonlinearities of the slice-selective pulse was implemented by minimizing deviations between the B_1^+ maps obtained using the 2D STEAM and 3D AFI methods on a head-sized gel phantom. This calibration procedure was performed only once prior to in vivo scanning and the whole central volume of the phantom was used (instead of a small central region of interest [ROI], as described in Helms et al. (18)). For in vivo scanning, three consecutively acquired B_1^+ maps were averaged in order to reduce instabilities due to the spurious occurrence of postsystolic cerebrospinal fluid flow through the image slices and head movements. As a result, one single B_1^+ map was produced with a reduced level of physiologic artifacts.

Reference 2D DAM Method

A reference B_1^+ map was acquired on each subject based on the application of a nonselective presaturation RF pulse followed by a slice-selective excitation pulse, similarly to the (saturation) DAM method introduced by Sled and Pike (24). Flip angle maps were calculated from the image intensities (S_1 and S_2) obtained for two values α_1 and α_2 of the presaturation flip angle:

$$\alpha_1 = \frac{1}{2}\arccos\left(\frac{S_2 + S_1}{2S_1}\right) \qquad [5]$$

with $\alpha_2 = 3 \times \alpha_1$. Signal was acquired using a multislice 2D EPI readout in order to reduce the scan time. Geometric distortions of the DAM B_1^+ maps were corrected using the unwarping procedure described in Fig. 1 for the 3D

2D STEAM Method

This rapid method is based on multislice single-shot STEAM MRI exploiting the signal dependence on the flip angle of the second ("flip back") pulse (18). Relative deviations of the flip angle from the nominal value are given by the spatially dependent factor f_T according to:

EPI method. Since the local flip angles were derived from variations of the nonselective presaturation pulse, any errors associated with slice selection were avoided. Complete relaxation of the magnetization was allowed between each repetition (i.e., $TR \geq 5 \times T_1$). The B_1^+ maps obtained from the 3D AFI, 3D EPI, and 2D STEAM methods were compared to those obtained from the 2D DAM method. Although the 2D DAM method does not constitute a true gold standard, the results from this comparison were used to assess the accuracy of the methods under study.

MATERIALS AND METHODS

Data were acquired on eight healthy volunteers (seven males, mean age 34 years), using a 3T whole-body Magnetom TIM Trio (Siemens Healthcare, Erlangen, Germany), operated with a body transmit coil and a 12-channel head-only receive coil. The study was approved by the local ethics committee, and written informed consent was obtained from the subjects prior to scanning. Four successive acquisitions of the 3D AFI, 3D EPI, and 2D STEAM methods were recorded on each subject within one scanning session in order to assess the reproducibility of these methods. The image resolution was $4 \times 4 \times 4$ mm^3 for all three methods. Due to its long acquisition time, the reference DAM scan was acquired only once on each subject, with an image resolution of $3 \times 3 \times 10$ mm^3.

3D AFI Method

Image acquisition was implemented with the following parameters: matrix size = $64 \times 60 \times 48$, field of view = $256 \times 240 \times 192$ mm^3, echo time (TE) = 3.13 ms. A Hamming-filtered sinc RF pulse with a nominal time-bandwidth product of 1 was used for spin excitation, with a duration of 500 μs and nominal flip angle $\alpha = 60°$. Spoiling of the magnetization was implemented using the modified spoiling scheme by Nehrke (25), with a phase increment of $\varphi = 129.3°$ and spoiler gradients with an amplitude of 26 mT/m and durations of 1/3 ms for TR$_1$/TR$_2$, based on simulation results of RF spoiling in FLASH acquisitions similar to simulations described in Preibisch and Deichmann (29). Diffusion weighting with reduced sensitivity to physiological artifacts was achieved by "three-lobes" flow-compensated gradient pulses with an amplitude of 26 mT/m and duration of

10.5 ms (with relative durations 1:2:1) (30). This corresponds to a diffusion damping of d $\sim 6.10^{-2}$, assuming a diffusion coefficient D $= 8.10^{-4}$ mm^2 sec^{-1} and neglecting the contribution of higher-order coherence pathways (25,31). We set TR$_1$ to 50 ms, the minimum achievable value due to the duration of the flow-compensated gradients. We set TR$_2$ to 150 ms in order to keep the acquisition time below 5 min. Parallel imaging (GRAPPA reconstruction, acceleration factor 3, 18 reference lines) was used in the phase direction, and partial Fourier (factor 6/8) was applied in the partition direction, yielding a total acquisition time of 4 min 12 sec.

3D EPI Method

Image acquisition was implemented with the following parameters: matrix size $= 64 \times 48 \times 48$, field of view $= 256 \times 192 \times 192$ mm^3 (17% oversampling along the partition direction), TE$_{SE}$/TE$_{STE}$/TM/TR $= 33.2/66.73/33.53/500$ ms. A Hamming-filtered sinc RF pulse with nominal time-bandwidth product of 12 was used for spin excitation, with a duration of 4ms and nominal flip angle $\alpha = 90°$. The duration of the rectangular SE and STE pulses was set to 700 μs. The respective flip angles for the SE/STE pulses were varied between 160°/80° and 200°/100° in steps of 10°/5°. The total experimental time was 2 min 20 sec. An additional B_0 map was acquired on each subject, as described in Weiskopf et al. (32), adding an extra 2 min of scan time. In the postprocessing of the B_1^+ maps, voxels whose fit exhibited more than 5% error and/or where the local B_0 deviation exceeded 110 Hz were replaced using the padding procedure described in the Theory section.

2D STEAM Method

Image acquisition was implemented with the following parameters: matrix size $= 64 \times 48$, field of view $= 256 \times 192$ mm^3, TE/TM/TR $= 6/30/24103$ ms. Fifty-six slices were selected, with a thickness of 2.9 mm and a distance factor of 38%, resulting in a gap of ~1.1 mm. Hamming-filtered sinc RF pulses with a time-bandwidth product of 2 and duration of 1280 μs were used for spin excitation and "flip-back". A shorter duration of 800 μs was used for signal readout. The nominal flip angles were kept constant at 90° and 12° for the excitation and readout pulses, respectively, and set to $\alpha_1/\alpha_2 = 60°/100°$ for the "flip-back" pulse. The acquisition time for one volume was 24 sec. Three successive volumes were acquired for averaging, leading to an overall acquisition time of 2 min 24 sec per averaged map. Calibration values $\alpha_{max} = 1.5755$ and q $= 0.6688$ were used in the following analyses. The deviation of these values from those of the original calibration method is attributed to differences in pulse shape of the "flip-back" pulses (18).

Reference DAM Method

Image acquisition was implemented with the following parameters: gradient-echo EPI readout with 12 slices, slice thickness/gap $= 5$ mm/5 mm, matrix size $= 64 \times 64$, field of view $= 192 \times 192$ mm^3, effective resolution of $3 \times 3 \times 10$ mm^3, TE $= 25$ ms, and TR $= 25$ sec to allow for complete relaxation of the magnetization between the scans. Rectangular RF pulses were used for presaturation of the magnetization with a duration of 500 μs. The nominal flip angle values of the presaturation pulse were $\alpha_1/\alpha_2 = 22°/66°$, separated by a factor 3 in order to increase the signal difference between the two images and enhance the signal-to-noise ratios in the resulting B_1^+ map. Spin excitation was implemented using slice-selective sinc RF pulses with a duration of 2560 μs (nominal flip angle value: $\alpha = 90°$). The total acquisition time was 10 min.

Data Analysis

All data processing was performed using MatLab (The MathWorks Inc., Natick, MA), version 7. This included the use of SPM8 (www.fil.ion.ucl.ac.uk) for data conversion, brain extraction, coregistration, and reslicing of the individual B_1^+ maps. B_0 maps were processed with a modified version of the SPM fieldmap toolbox (28). Custom-made MatLab scripts were used for estimation of the B_1^+ maps from the acquired datasets and for data analysis.

Flip angle values in all B_1^+ maps were calculated as a percentage of the nominal flip angle (in percentage units = p.u.). This allowed for straightforward comparison of the results between the methods, assuming a linear relationship between nominal and local flip angles. B_1^+ maps were smoothed with an 8 mm full-width-at-half-maximum gaussian kernel prior to further analysis. For each B_1^+ mapping method, the voxelwise mean and standard deviation (SD) across the four repeated measurements were calculated. The map of differences between the voxelwise mean for each technique and the DAM reference values was used to determine the accuracy or bias of each method. The SD maps were used as indicators of reproducibility or precision.

To quantitatively compare the different methods, the voxelwise means, standard deviations, and differences from the reference were averaged over an ROI in the central part of the brain, providing values B_1-mean, B_1-SD and B_1-bias, respectively, for each technique and each subject. The ROI was created on an individual basis using the same automated procedure for all subjects: the short TE magnitude T_1-weighted image acquired as part of the B_0 map acquisition was segmented into tissue probability maps (33). Cerebrospinal fluid, gray matter, and white matter tissue segments were then combined to form a brain mask. Morphologic operators were used to erode the mask by 10 voxels followed by smoothing and thresholding to create a region located well inside the brain. Repeated-measures analysis of variance (ANOVA) (SPSS, version 17.0; IBM Company, New York, NY) of B_1-mean and B_1-SD was used to test for significant differences between the sequences. Standard post hoc paired t tests were performed to explore any difference further. Statistical significance was assessed at a threshold of $P < 0.05$.

RESULTS

Figure 2a-d shows sagittal and axial views of typical B_1^+ uniformity patterns acquired using the DAM (Fig. 2a,b)
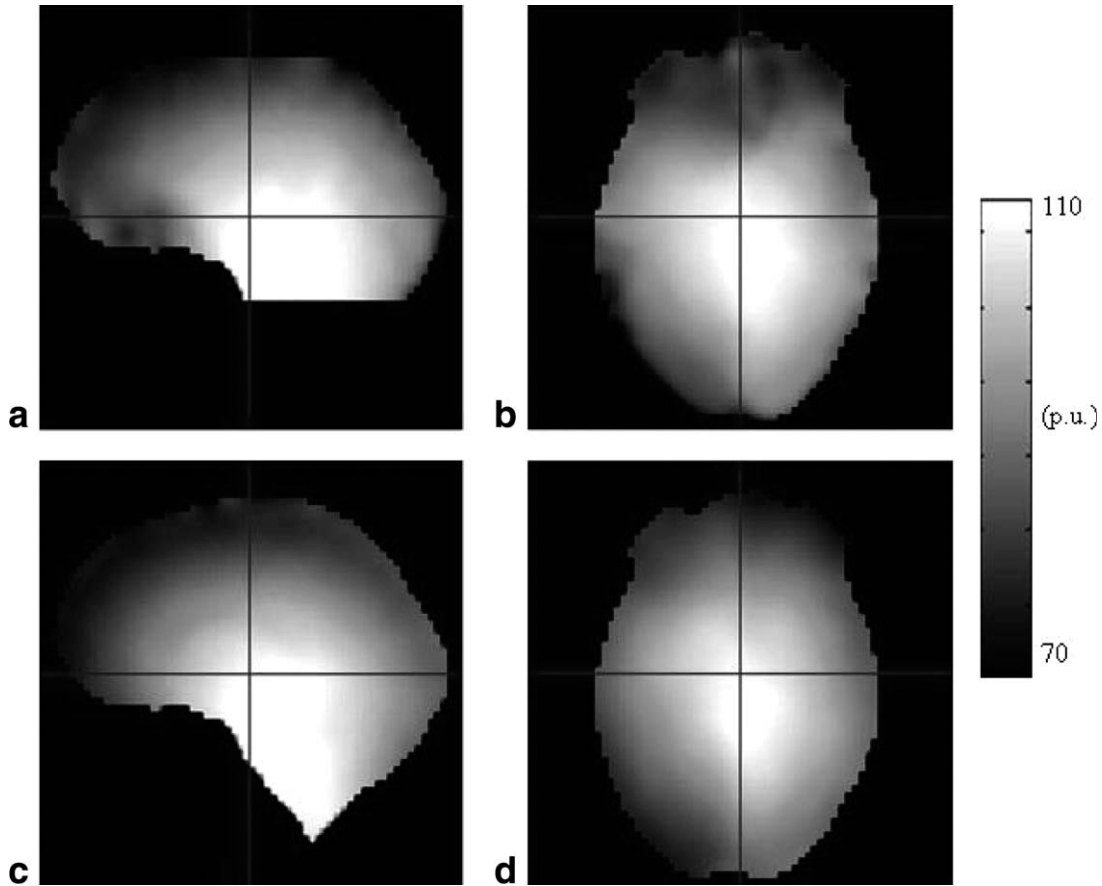
FIG. 2. Sagittal and axial views of B_1^+ maps for a single subject acquired using the DAM **(a,b)** and 3D AFI **(c,d)** methods. Note the susceptibility-induced artifacts in the orbitofrontal cortex in the DAM method; 184 × 152 mm (600 × 600 DPI).

and 3D AFI (Fig. 2c,d) methods for a single subject. Local flip angles vary between ~70 p.u. and 120 p.u. of the nominal value over the brain volume. Note that little "shine-through" of brain structure into the B_1^+ maps (an indication of inaccurate B_1^+ values) is apparent even around the ventricles, reflecting the low sensitivity of these methods to the long T_2 times of cerebrospinal fluid and to flow effects. A diagonal pattern of B_1^+ nonuniformity is present in the axial views. This effect, detected by all methods presented here, is due to the interaction between the subject and the B_1^+ field (34). In the DAM B_1^+ maps, off-resonance artifacts can be seen in the region of the orbitofrontal cortex.

Figure 3a-c shows sagittal and axial slices through typical voxelwise mean B_1^+ maps acquired using each method under study. For the 3D AFI and 3D EPI methods, only smooth variations are present and no "shine-through" of brain structure is apparent. On the 2D STEAM B_1^+ maps, the latter artifact is visible at the level of the third ventricle due to flow effects. Voxelwise difference images between the methods under study and the reference method are shown in Fig. 3d-f. Overall, the 3D EPI method overestimates the flip angles compared to the reference method, whereas the 3D AFI method underestimates them. All difference maps show "shine-through" of the ventricles of amplitude ~1 p.u. Large difference values are visible for all methods in the orbito-

frontal cortex. Both effects arise from artifacts in the reference DAM method, as shown in Fig. 2a,b, and are not apparent in pairwise comparisons of the three methods (not shown). Artifacts are also visible in the outer parts of the brain in all difference images due to partial-volume effects arising from the large slice thickness used for the reference method. Figure 3g-i shows the voxelwise standard deviations of the B_1^+ maps obtained from four repetitions of each of the methods. While the 3D EPI method was most stable (SD <1.5 p.u.), significant instabilities were found for the 2D STEAM method (SD >5 p.u.), particularly at the location of the ventricles and at the base of the brain where high blood flow and pulsating cerebrospinal fluid flow are present. The results shown in Fig. 3 were representative of all subjects.

A quantitative comparison across subjects was performed by averaging the B_1^+ results over an ROI covering the central regions of the brain, where the reference DAM method is expected to perform optimally. This ROI is illustrated by the red contour in Fig. 3. The means and standard deviations of B_1-mean values across subjects were 99.3 ± 1.7, 104.7 ± 1.6, 101.9 ± 2.1, and 100.7 ± 1.6 p.u. for the 3D AFI, 3D EPI, 2D STEAM, and reference methods, respectively. Repeated measures ANOVA showed a dependence of B_1-mean on the B_1^+ mapping method (F = 84, df = (3,21), P < 0.001), although these differences were relatively small and did
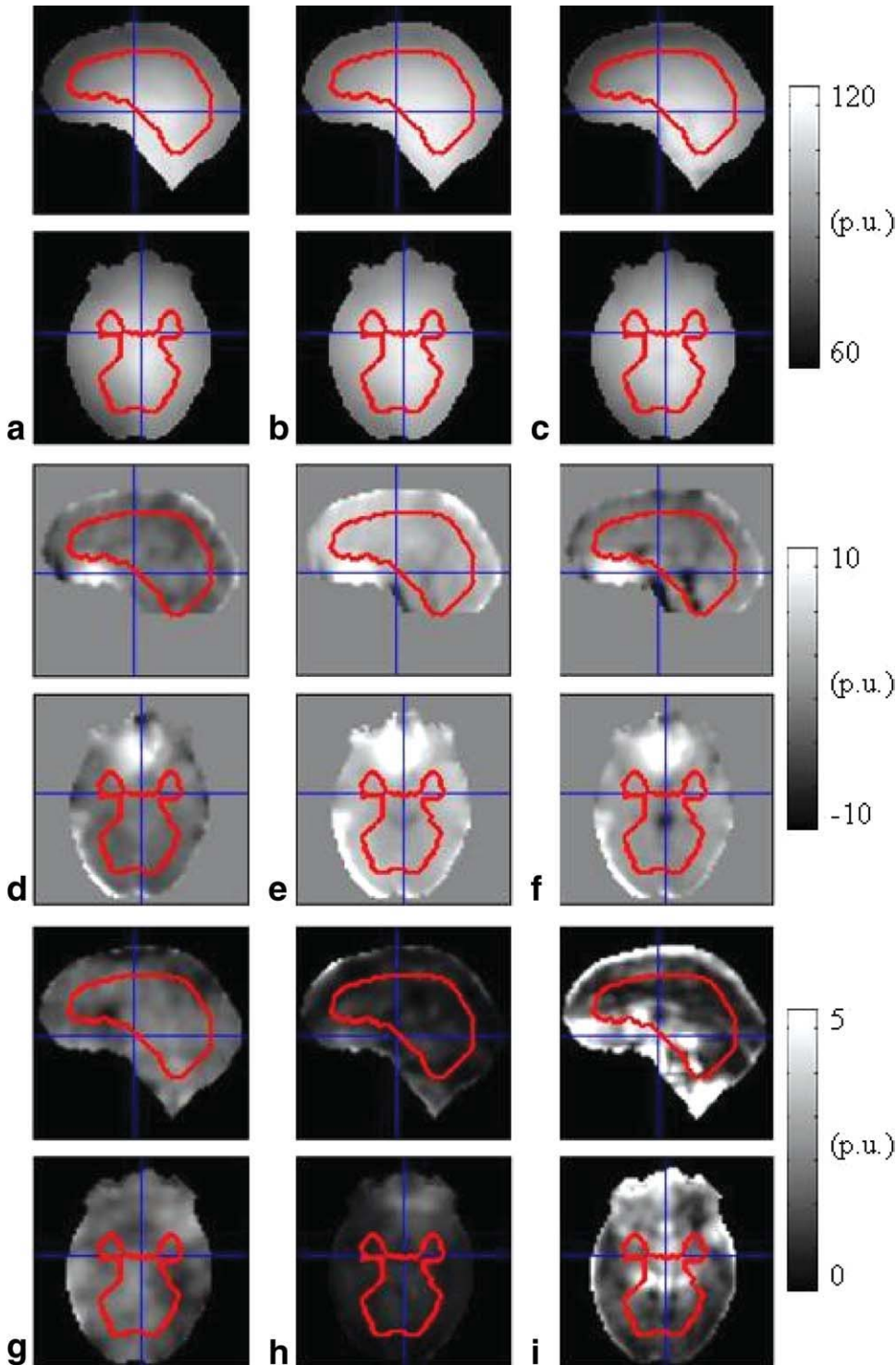
FIG. 3. Sagittal and axial views for a single subject for the 3D AFI **(a,d,g)**, 3D EPI **(b,e,h)**, and 2D STEAM **(c,f,i)** B_1^+ mapping methods. **a–c**: B_1^+ maps obtained using each of the methods; **(d–f)** difference images with the reference DAM method; **(g–i)** standard deviation maps taken over four successive repetitions of each method. The red outlines illustrate the ROI used in our study; 164 $\times$ 254 mm (600 $\times$ 600 DPI).

not exceed 5 p.u. Post hoc paired t tests showed statistically significant differences between all methods (t >5.9, df = 7, P < 0.001), except for 2D STEAM versus 2D DAM (t $\approx$ 2.3, df = 7, P > 0.05).

Figure 4 shows the B_1-bias values for each method and each subject, providing a measure of accuracy of the methods. The means and standard deviations of B_1-bias across subjects were −1.4 $\pm$ 0.7 p.u., 4.0 $\pm$ 0.2 p.u., and 1.2 $\pm$ 1.5 p.u. for the 3D AFI, 3D EPI, and 2D STEAM methods, respectively. An outlier subject in the 2D STEAM dataset (#4) led to a wider range of B_1-mean values. Omitting the outlier subject in the 2D STEAM
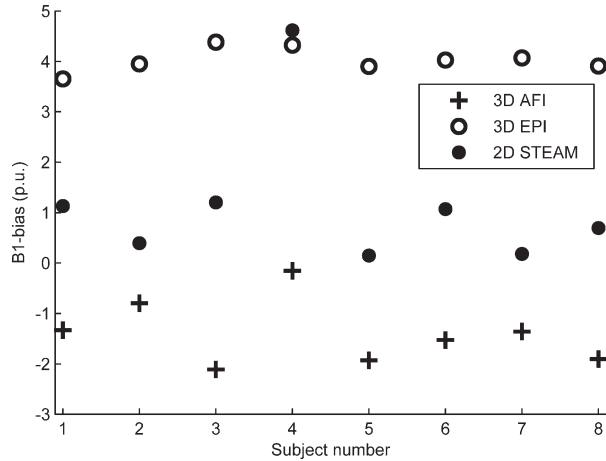
FIG. 4. Bias/accuracy. Flip angle differences between each of the methods under study and the reference DAM technique averaged over the ROI (B_1-bias); 103 × 71 mm (600 × 600 DPI).

dataset decreased the corresponding mean B_1-bias to 0.7 ± 0.5 p.u.

Figure 5 shows B_1-SD for each method and each subject, providing a measure of the reproducibility/precision of the methods. The means and standard deviations of B_1-SD values across subjects were 1.6 ± 0.2, 0.4 ± 0.2, and 0.9 ± 0.3 p.u. for the 3D AFI, 3D EPI, and 2D STEAM methods, respectively. The standard error for each mean B_1-SD value is in good agreement with the SD of each B_1-bias value (i.e., comparing Figs. 4 and 5), which shows the coherence of our results. Repeated-measures ANOVA tests showed a dependence of B_1-SD on the B_1^+ mapping methods (F = 80, df = (2,14), $P <$ 0.001). Post hoc paired t tests showed statistically significant differences between all B_1-SD distributions (t > 5.9, df = 7, $P <$ 0.001).

DISCUSSION

We optimized and compared three published methods for rapid mapping of the B_1^+ field in the human head at 3T: 3D AFI (22), 3D EPI (23), and 2D STEAM (18). In order to assess the accuracy of the techniques under study, results were compared to the 2D DAM method (24), chosen as a reference in the experiment design. Before optimization, each B_1^+ mapping method showed specific artifacts that were addressed in this study. After optimization, results were found within 5 p.u. agreement with the reference B_1^+ maps. Standard deviations over repetitions were below 2 p.u. The overall errors were therefore found small compared to the typical variations of ~50 p.u. observed at 3T across the brain.

3D AFI Method

The signal equation for the dual-excitation FLASH experiment used in 3D AFI does not account for residual transverse coherences (29). Reducing these by choice of small flip angles is not an option, because the separation of flip angle bias and relaxation becomes ill conditioned, as shown by the rational approximation of the steady-state signals (11,35). For the large flip angle (60°) used

here, the addition of flow-compensating diffusion damping gradients reduced bias due to incomplete spoiling of transverse coherences while minimizing the flow and motion sensitivity of the method, an approach similar to the one used for steady-state free-precession sequences in Ding et al. (36).

Sufficient diffusion spoiling required long gradient pulses and therefore longer TR values (50/150 ms), resulting in an increased acquisition time. As a result of the increased TR values, misestimation of the flip angles from longitudinal relaxation effects may reach up to ~1 p.u. locally, according to simulations similar to those by Yarnykh (22). Further spoiling of the transverse coherences would require longer diffusion gradients since the spoiler amplitudes cannot be significantly increased further on a typical whole-body clinical scanner. This would result in longer TR values and an increased acquisition time and flip angle bias due to longitudinal relaxation effects.

3D EPI Method

Distortion correction mitigated spatial distortions of the B_1^+ maps obtained using the 3D EPI method by two voxels or more in areas such as the inferior temporal lobe and orbitofrontal cortex. The padding procedure (RMS and B_0) corrected B_1^+ in 3.9 ± 0.7% of the voxels in the flip angle maps by an amount of 3.4 ± 0.8 p.u. averaged across subjects. The brain regions affected by RMS-padding were mainly near the superior sagittal sinus and the circle of Willis, where large blood vessels are present (~ 3.8% of the brain volume). Brain vasculature may therefore be the main contributor to these errors on the flip angle estimates. B_0-padding only affected the orbitofrontal cortex due to the high susceptibility gradients in this region (~0.6% of the brain volume). If applied on areas of larger size, padding might fail to reflect accurately the topological features of the true B_1^+ field. The threshold for B_0 padding depends on the SE/STE RF pulses used experimentally and may need to be recalibrated if these are changed.
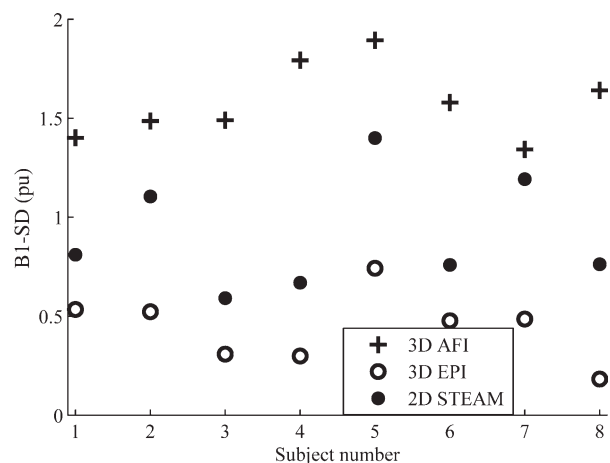

FIG. 5. Reproducibility/precision. Standard deviation of four successive repetitions of each B_1^+ mapping method averaged over the ROI (B_1-SD); 103 × 72 mm (600 × 600 DPI).

Table 1
Summary of Characteristics for the Three B_1^+ Mapping Methods Presented in This Study

	3D AFI	3D EPI	2D STEAM
B_1-bias (p.u.)	-1.4 ± 0.7	4.0 ± 0.2	1.2 ± 1.5
B1-SD (p.u.)	1.6 ± 0.2	0.4 ± 0.2	0.9 ± 0.3
Calibration	No	No	Yes (of slice-selective pulse)
Postprocessing	No	Yes (correction of undistortions and off-resonance effects)	Yes (reduction of physiological noise)
Processing time[a]	<5 sec	<2 min	<5 sec
Acquisition time	4 min 12 sec	2 min 20 sec + 2 min (B_0 map)	2 min 24 sec

[a]PC, Intel Xeon, 3.2 GHz, eight cores, 12-GB random-access memory (Dell Inc., Round Rock, TX).

The 3D EPI method showed the most reproducible results over repetitions and across subjects but the largest systematic bias compared to the reference DAM method. The origin of this systematic bias remains unclear. According to Jiru and Klose (23), the effect of longitudinal relaxation during the mixing time may not exceed ∼0.5 p.u. for the range of flip angles present within the ROI. Based on preliminary experiments on the effect of off-resonance on the B_1^+ maps, we found that only $3 \pm 1\%$ of the voxels within the ROI were biased by more than 0.5 p.u. due to off-resonance, averaged across subjects. For these voxels, the average off-resonance bias was 0.65 ± 0.07 p.u., small compared to the ∼4 p.u. systematic bias observed over the ROI.

The precision of the method was largely determined by the number of nominal flip-angle values (23). However, additional acquisitions seemed unnecessary, since the current implementation already achieved the highest precision of all methods. For the data presented here, setting the threshold for RMS padding to 5 p.u. proved to be in general a good tradeoff between denoising the data sufficiently and minimal reduction of degrees of freedom in the dataset.

2D STEAM Method

For the 2D STEAM method, calibration of the nonlinearities of the slice-selective pulse was improved by cross-calibrating with an independent (AFI) B_1^+ mapping method. The calibration was implemented on the entire volume of a gel phantom in order to obtain more reliable results across the whole range of flip angles and reduced sensitivity to fitting errors in the reference curve. The results of the calibration were used as a multiplicative factor of the local flip angle (18), removing any systematic bias between the two methods. As a result, a similar level of accuracy between the two methods might be expected on human subjects. The high time efficiency of the 2D STEAM method permitted averaging over three B_1^+ maps based on successive acquisitions, yielding an averaged B_1^+ map with a reduced level of instability.

Despite averaging, local instabilities beyond 5 p.u. persisted due to physiology-related artifacts. Averaging over a higher number of acquisitions might be desirable as the total acquisition time for three repetitions was still shorter than for the other methods (∼2.5 min instead of ∼4.5 min). Averaging of image intensities obtained for each value of the flip-back pulse instead of averaging the B_1^+ maps (as done here) may reduce instabilities further. Reduction of in-flow artifacts may alternatively be achieved by physiologic triggering. Fitting a sine curve to six different flip-back angles (37) may reduce the sensitivity of the method to spurious artifacts, simplify the calibration, and allow the use of a padding procedure similar to that of the 3D EPI method. Here, the original method and the quadratic approximation of the flip angle dependence were retained to enable the comparison with the other two-point methods. The presence of an outlier subject (#4) in the STEAM dataset for which higher flip angles were measured consistently across repetitions remains unexplained.

Comparison of the Methods

The main findings of this comparison study are summarized in Table 1. All optimized methods provided B_1^+ maps with errors less than 5 p.u. for a total scan time of <4.5 min. The 3D EPI method showed the highest reproducibility with B_1-SD <0.7 p.u. The intrasubject SD of the 2D STEAM varied significantly across the brain due to its sensitivity to flow. The 3D AFI method had the lowest reproducibility (B_1-SD <1.9 p.u.), but high compared to the 50 p.u. variations of the flip angles across the brain. Deviations from the DAM reference method were found between 1 and 2 p.u. for the 3D AFI and 2D STEAM methods. The STEAM cross-calibration method implemented here likely contributed to the similar accuracy found for both methods. The accuracy of the 3D EPI method was lower, with ∼4 p.u. deviation from the reference. If necessary, this bias could be reduced by cross-calibration with a reference B_1^+ mapping method, similar to the calibration performed for the 2D STEAM method.

In principle, the 2D STEAM method is the fastest and can generate a B_1^+ map in only 2×24 sec. The averaging of three acquisitions to reduce in-flow effects brought the total scan time to about 2.5 min. Despite averaging, this method remained faster than the 3D AFI method that had a scan time of ∼4.5 min, even with 3-fold GRAPPA acceleration and partial Fourier sampling. The scan time for the 3D EPI was approximately 2.5 min. For this method, implementation of parallel imaging along the phase and partition directions would significantly reduce the acquisition time and the amount of spatial distortions in the EPI images. An additional B_0 map was necessary for correction of off-resonance artifacts, adding another ∼2 min to the overall scan time. Since B_0 maps are frequently acquired for different purposes in MRI examinations, this may often not be an additional overhead. Furthermore the B_0 mapping can be made faster,

since large coverage (beyond the B_1^+ map) and rather long TRs were used.

The implementation of the 3D AFI method was straightforward, with minimal postprocessing and no need for calibration. In contrast, the 3D EPI method required postprocessing steps, including unwarping, masking, and padding of the B_1^+ maps. The 2D STEAM method relied on an extra (one-time) calibration for non-linearities due to the slice-selective RF pulses to maximize its accuracy but otherwise required minimal postprocessing.

The 3D AFI method required comparably higher gradient power than the 3D EPI and 2D STEAM methods since the flow-compensated spoilers were driven with high amplitudes and duty cycle to keep the TR minimal. This puts high demand on the scanner hardware and may also impact on subjects' compliance due to mechanical movement (similar to diffusion imaging).

Considerations

The 2D DAM method is conceptually simple and insensitive to longitudinal relaxation times and slice-selection nonlinearities. Therefore, it was chosen as a reference in order to assess the accuracy of the 3D AFI, 3D EPI, and 2D STEAM methods despite its low resolution, long acquisition time, and sensitivity to off-resonance effects. While an ROI covering the entire brain would enable a more complete comparison between the methods, we focused on an ROI inside the brain and covering most of the brain volume, where the reference DAM method was seen to perform optimally. As a result, the impact of physiologic noise sources present in outer brain regions (e.g., blood flow) was excluded from the study.

Fast whole-brain B_1^+ mapping methods as presented here are currently not readily available on clinical MR systems and still need to be implemented using pulse-sequence programming on site. All methods were implemented here on a system with a high-power RF amplifier (35 kW) and gradient system (slew rate up to 200 mT/m/ms (38)). The sequence parameters may need to be adapted when implemented on another system, possibly affecting the quality of the results. In particular, the RF pulse duration should be minimal to reduce off-resonance sensitivity while the RF amplifier should still operate in the linear regime. For the 3D sequences, Hamming-filtered sinc pulses were used for slab-selective excitation in order to achieve an optimal slice profile. A sufficient slab thickness might be desirable in order to minimize inflow effects, and oversampling in the partition-encoding direction should be used to reduce potential wraparound. High gradient power enables fast EPI readouts, reducing geometric distortions and the mixing/echo times in the 3D EPI method. It also allows for efficient spoiling in the 3D AFI method while minimizing TR. Relaxation times and off-resonance effects should be considered while implementing the methods at different B_0 field strengths. Also, the use of head transmit RF coils would increase in-flow effects compared to the body transmit coil used here since the nonselective RF pulses used for determining the local transmit field would saturate flowing blood outside the

brain less efficiently (39). Also, localized surface coils may enhance signal from the scalp that can increase the amplitude of motion artifacts (40).

Although all B_1^+ mapping methods were optimized and validated for brain imaging, they may be used to scan other organs. For example, the intrinsic robustness of the 3D AFI method against susceptibility-related distortions makes it a good candidate for B_1^+ mapping in areas affected by susceptibility artifacts (e.g., near bones), which might be challenging for the 3D EPI method. Large vessels and blood flow (e.g., in the abdomen and thorax) are expected to exacerbate the flow artifacts in the 2D STEAM method.

CONCLUSION

The accuracy and precision of three B_1^+ mapping methods—3D AFI, 3D EPI, and 2D STEAM—were assessed in the context of human brain imaging at 3T. The acquisition time for all three methods was below 5 min. For each method, the observed artifacts were mainly due to the specific sequence used for spatial encoding. Optimization of these methods yielded overall errors less than 5 p.u. in the central regions of the brain, small compared to the typical variations of ~50 p.u. in the B_1^+ field observed across the brain at 3T. The choice of a particular method for routine B_1^+ mapping may depend on the properties of the B_1^+ maps required by the user. If high reproducibility is desired, the 3D EPI method is recommended. However, postprocessing is required for this method in order to correct for image distortions and flip-angle bias. The intrinsic robustness of the 3D AFI method against susceptibility-related distortions makes it a good candidate for B_1^+ mapping in areas affected by susceptibility artifacts and at higher fields. However, it poses rather high demands on the scanner hardware and requires a relatively long minimal scan time. If rapidity is of primary importance, the 2D STEAM method might be preferred. However, this method is most sensitive to physiologic artifacts and requires calibration using an independent method.

REFERENCES

1. Schepers J, van Osch MJ, Bartels LW, Heukels SN, Viergever MA, Nicolay K. The effect of B_1 field inhomogeneity and the nonselective inversion profile on the kinetics of FAIR-based perfusion MRI. Magn Reson Med 2005;53:1355–1362.
2. Samson RS, Wheeler-Kingshott CA, Symms MR, Tozer DJ, Tofts PS. A simple correction for B_1 field errors in magnetization transfer ratio measurements. Magn Reson Imaging 2006;24:255–263.
3. Venkatesan R, Lin WL, Haacke EM. Accurate determination of spin-density and T-1 in the presence of RF-field inhomogeneities and flip-angle miscalibration. Magn Reson Med 1998;40:592–602.
4. Wang D, Heberlein K, LaConte S, Hu X. Inherent insensitivity to RF inhomogeneity in FLASH imaging. Magn Reson Med 2004;52:927–931.

5. Deichmann R, Good CD, Turner R. RF inhomogeneity compensation in structural brain imaging. Magn Reson Med 2002;47:398–402.

6. Thomas DL, De Vita E, Deichmann R, Turner R, Ordidge RJ. 3D MDEFT imaging of the human brain at 4.7 T with reduced sensitivity to radiofrequency inhomogeneity. Magn Reson Med 2005;53:1452–1458.

7. Vovk U, Pernus F, Likar B. A review of methods for correction of intensity inhomogeneity in MRI. IEEE Trans Med Imaging 2007;26:405–421.

8. Collins CM, Li SZ, Smith MB. SAR and B-1 field distributions in a heterogeneous human head model within a birdcage coil. Magn Reson Med 1998;40:847–856.

9. Van den Berg CA, van den BB, Van de Kamer JB, Raaymakers BW, Kroeze H, Bartels LW, Lagendijk JJ. Simultaneous $B_1 +$ homogenization and specific absorption rate hotspot suppression using a magnetic resonance phased array transmit coil. Magn Reson Med 2007;57:577–586.

10. Zhang Z, Yip CY, Grissom W, Noll DC, Boada FE, Stenger VA. Reduction of transmitter B_1 inhomogeneity with transmit SENSE slice-select pulses. Magn Reson Med 2007;57:842–847.

11. Helms G, Dathe H, Dechent P. Quantitative FLASH MRI at 3T using a rational approximation of the Ernst equation. Magn Reson Med 2008;59:667–672.

12. Insko EK, Bolinger L. Mapping of the radiofrequency field. J Magn Reson A 1993;103:82–85.

13. Wang JH, Qiu ML, Constable RT. In vivo method for correcting transmit/receive nonuniformities with phased array coils. Magn Reson Med 2005;53:666–674.

14. Stollberger R, Wach P. Imaging of the active B_1 field in vivo. Magn Reson Med 1996;35:246–251.

15. Cunningham CH, Pauly JM, Nayak KS. Saturated double-angle method for rapid B_1^+ mapping. Magn Reson Med 2006;55:1326–1333.

16. Hoult DI. Solution of the Bloch equations in the presence of a varying B_1 field: approach to selective pulse analysis. J Magn Reson 1979;35:69–86.

17. Wang JH, Mao WH, Qiu ML, Smith MB, Constable RT. Factors influencing flip angle mapping in MRI: RF pulse shape, slice-select gradients, off-resonance excitation, and B_0 inhomogeneities. Magn Reson Med 2006;56:463–468.

18. Helms G, Finsterbusch J, Weiskopf N, Dechent P. Rapid radiofrequency field mapping in vivo using single-shot STEAM MRI. Magn Reson Med 2008;60:739–743.

19. Haacke EM, Brown RW, Thompson MR, Venkatesan R. Sequence design, artifacts and nomenclature: magnetic resonance imaging. Wiley-Liss, NY; 1999. 816 p.

20. Duyn JH, Yang Y, Frank JA, Mattay VS, Hou L. Functional magnetic resonance neuroimaging data acquisition techniques. Neuroimage 1996;4(3 pt 3):S76–S83.

21. Metzger GJ, Snyder C, Akgun C, Vaughan T, Ugurbil K, Van De Moortele PF. Local B_1+ shimming for prostate imaging with transceiver arrays at 7T based on subject-dependent transmit phase measurements. Magn Reson Med 2008;59:396–409.

22. Yarnykh VL. Actual flip-angle imaging in the pulsed steady state: a method for rapid three-dimensional mapping of the transmitted radiofrequency field. Magn Reson Med 2007;57:192–200.

23. Jiru F, Klose U. Fast 3D radiofrequency field mapping using echo-planar imaging. Magn Reson Med 2006;56:1375–1379.

24. Sled JG, Pike GB. Correction for B_1 and B_0 variations in quantitative T_2 measurements using MRI. Magn Reson Med 2000;43:589–593.

25. Nehrke K. On the steady-state properties of actual flip angle imaging (AFI). Magn Reson Med 2009;61:84–92.

26. Yarnykh VL. Optimal spoiling of the transverse magnetization in the actual flip-angle imaging (AFI) sequence for fast B_1 field mapping. In: Proceedings of the 16th Annual Meeting of ISMRM, Toronto, Canada, 2008, p329.

27. Akoka S, Franconi F, Seguin F, Lepape A. Radiofrequency map of an NMR coil by imaging. Magn Reson Imaging 1993;11:437–441.

28. Hutton C, Bork A, Josephs O, Deichmann R, Ashburner J, Turner R. Image distortion correction in fMRI: a quantitative evaluation. Neuroimage 2002;16:217–240.

29. Preibisch C, Deichmann R. Influence of RF spoiling on the stability and accuracy of T1 mapping based on spoiled FLASH with varying flip angles. Magn Reson Med 2009;61:125–135.

30. Bernstein MA, King KF, Zhou XJ. Handbook of MRI pulse sequences, Gradient moment nulling, p 331–349, Elsevier Academic Press; London: 2004.

31. Le Bihan D. Looking into the functional architecture of the brain with diffusion MRI. Nat Rev Neurosci 2003;4:469–480.

32. Weiskopf N, Hutton C, Josephs O, Deichmann R. Optimal EPI parameters for reduction of susceptibility-induced BOLD sensitivity losses: a whole-brain analysis at 3 T and 1.5 T. Neuroimage 2006;33:493–504.

33. Ashburner J, Friston K. Multimodal image coregistration and partitioning—a unified framework. Neuroimage 1997;6:209–217.

34. Sled JG, Pike GB. Standing-wave and RF penetration artifacts caused by elliptic geometry: an electrodynamic analysis of MRI. IEEE Trans Med Imaging 1998;17:653–662.

35. Helms G, Dathe H, Kallenberg K, Dechent P. High-resolution maps of magnetization transfer with inherent correction for RF inhomogeneity and T1 relaxation obtained from 3D FLASH MRI. Magn Reson Med 2008;60:1396–1407.

36. Ding S, Trillaud H, Yongbi M, Rolett EL, Weaver JB, Dunn JF. High resolution renal diffusion imaging using a modified steady-state free precession sequence. Magn Reson Med 1995;34:586–595.

37. Helms G. A precise and user-independent quantification technique for regional comparison of single volume proton MR spectroscopy of the human brain. NMR Biomed 2000;13:398–406.

38. Price D, Delakis I, Renaud C, Dickinson R. 3T MRI systems: comparative report on four MRI systems. London: Centre for Evidence-based Purchasing; 2007.

39. Deichmann R, Schwarzbauer C, Turner R. Optimisation of the 3D MDEFT sequence for anatomical brain imaging: technical implications at 1.5 and 3 T. Neuroimage 2004;21:757–767.

40. Howarth C, Hutton C, Deichmann R. Improvement of the image quality of T1-weighted anatomical brain scans. Neuroimage 2006;29:930–937.